Distinguishing type II focal cortical dysplasias from normal cortex: A novel normative modeling approach

Kathryn Snyder [a], Emily P. Whitehead [b], William H. Theodore [c], Kareem A. Zaghloul [d], Souheil J. Inati [e], Sara K. Inati [a],[*]

[a] EEG Section, Office of the Clinical Director, NINDS, National Institutes of Health, United States
[b] Cadwell, Kennewick, WA, United States
[c] Clinical Epilepsy Section, NINDS, National Institutes of Health, United States
[d] Surgical Neurology Branch, NINDS, National Institutes of Health, United States
[e] Office of the Clinical Director, NINDS, National Institutes of Health, United States

ABSTRACT

Objective: Focal cortical dysplasias (FCDs) are a common cause of apparently non-lesional drug-resistant focal epilepsy. Visual detection of subtle FCDs on MRI is clinically important and often challenging. In this study, we implement a set of 3D local image filters adapted from computer vision applications to characterize the appearance of normal cortex surrounding the gray-white junction. We create a normative model to serve as the basis for a novel multivariate constrained outlier approach to automated FCD detection.

Methods: Standardized MPRAGE, T_2 and FLAIR MR images were obtained in 15 patients with radiologically or histologically diagnosed FCDs and 30 healthy volunteers. Multiscale 3D local image filters were computed for each MR contrast then sampled onto the gray-white junction surface. Using an iterative Gaussianization procedure, we created a normative model of cortical variability in healthy volunteers, allowing for identification of outlier regions and estimates of similarity in normal cortex and FCD lesions. We used a constrained outlier approach following local normalization to automatically detect FCD lesions based on projection onto the mean FCD feature vector.

Results: FCDs as well as some normal cortical regions such as primary sensorimotor and paralimbic regions appear as outliers. Regions such as the paralimbic regions and the anterior insula have similar features to FCDs. Our constrained outlier approach allows for automated FCD detection with 80% sensitivity and 70% specificity.

Significance: A normative model using multiscale local image filters can be used to describe the normal cortical variability. Although FCDs appear similar to some cortical regions such as the anterior insula and paralimbic cortices, they can be identified using a constrained outlier detection approach. Our method for detecting outliers and estimating similarity is generic and could be extended to identification of other types of lesions or atypical cortical areas.

1. Introduction

Focal cortical dysplasia (FCD) is a relatively common cause of drug-resistant focal epilepsy, and particularly of MRI negative (MRI-) epilepsy. Approximately 15–25% of patients being evaluated for epilepsy surgery have apparently normal MRIs; FCD is diagnosed pathologically in 25–50% of these patients (Blumcke et al., 2017; Lerner et al., 2009; Bien et al., 2009). Because post-operative seizure outcomes are significantly worse in MRI- compared to MRI positive (MRI+) patients (Téllez-Zenteno et al., 2010), improved identification of subtle FCDs is of great clinical importance as it may lead to better surgical outcomes.

FCDs are variable in their histopathological and radiographic appearances. Pathological abnormalities range from cortical dyslamination in FCD type I, to the presence of large dysmorphic neurons in type IIa (FCDIIa), and balloon cells and more prominent dysmyelination in type IIb (FCDIIb) (Blümcke et al., 2011). FCD type I lesions are typically difficult to identify radiologically, most often consisting of cortical thinning and lobar hypoplasia, at times with blurring of the gray-white

junction and changes in T_1- or T_2-weighted image intensity. FCD type II lesions are more easily identified on MRI, with typical findings consisting of increased cortical thickness, blurring of the gray-white junction, FLAIR/ T_2 hyperintensity (including the transmantle sign in FCD type IIb), and alterations in gyrification patterns (Adler et al., 2017a; 2017b;; Kini et al., 2016). These findings, however, appear inconsistently within and across lesions (Hong et al., 2017) and are often subtle, with up to 80% of small bottom-of-sulcus dysplasias being missed on routine visual inspection (Besson et al., 2008).

To aid with detection of subtle FCD lesions, a number of postprocessing methods have been developed. These range from creation of synthetic contrasts to highlight areas of interest (such as the Morphometric Analysis Program (MAP) (Huppertz et al., 2005)), to machine-learning based fully automated detection methods such as those described by (Adler et al., 2017a; 2017b;; Ahmed et al., 2015; Hong et al., 2014). Across these methods, two key challenges have been 1) selection of optimal features to describe FCD lesions, and 2) accounting for variability within and across FCD lesions, as well as in normal cortex. While a wide variety of features have been investigated, most methods have used features derived from either voxel-based morphometry (Huppertz et al., 2005; Martin et al., 2017) or surface-based morphometry (SBM) (see review in (Kini et al., 2016)). Higher-order textural features or local statistics used to describe the local characteristics of patches within an image, although well-described in computer vision applications (for example, (Portilla et al., 2003)), have only occasionally been applied in biomedical imaging (for examples, see (Joyseeree et al., 2018; Wang et al., 2018; Zacharaki et al., 2009)), and even less often for FCD detection (Antel et al., 2003, Bernasconi et al., 2001).

In this work, we describe a novel approach for describing and detecting FCD lesions. We first create a model to describe the normal variability observed along the cortical sheet in healthy volunteers. This model is based on an implementation of 3D multiscale rotationally-invariant local image features across multiple MR contrasts, similar to those that have been previously shown to efficiently represent the local statistics of natural images (Simoncelli and Olshausen, 2001). We use these features to create a latent representation of this normative data that allows for straightforward outlier detection in our multivariate feature space. In healthy volunteers, we show that our outlier detection approach identifies cortical regions that are known to have atypical underlying cytoarchitectonic and myelination patterns such as paralimbic and primary sensorimotor cortices. In patients, most FCD lesions also appear as outliers, but are similar in their underlying features to some normally atypical regions. We show that a constrained outlier detection approach in combination with local normalization allows for automated detection of FCDs.s

2. Materials and methods

2.1. Study participants

From our surgical epilepsy imaging database, we retrospectively identified 15 consecutive patients undergoing presurgical evaluation for drug-resistant focal epilepsy from 2014 to 2019 with 1) radiologically apparent (MRI+) or histologically proven (MRI+ or MRI-) FCDs; and 2) our standard 3 T MRI epilepsy structural imaging protocol. Patients were excluded if they underwent other MR imaging protocols or had low image quality on visual inspection. The control group consisted of 30 healthy volunteers (HVs) scanned using the same imaging protocol with no previous history of neurologic, psychiatric, or other significant medical illnesses that may affect the central nervous system. Data were collected at the National Institutes of Health (NIH) Clinical Center (Bethesda, MD). All participants were enrolled in an Institutional Review Board-approved research protocol; informed consent was obtained from all participants.

2.2. Lesion labels

For MRI+ patients, lesions were traced in the volume using the Analysis of Functional NeuroImages (AFNI) software package (Cox, 1996) by an experienced neurologist using the T_1 weighted image, informed by the T_2 and FLAIR images when necessary. For MRI- patients, the postoperative T_1 was registered to the preoperative T_1 in the same manner as described below for T_2 and FLAIR images; the resected region was manually traced using AFNI. Lesion masks were mapped onto the smoothed white matter surface using AFNI's 3dVol2Surf function.

2.3. MRI acquisition protocol

All participants were scanned on a Philips Achieva 3 T MRI scanner in the NIH Clinical Center Radiology Department as follows: 1) 3D T_1 weighted MPRAGE (T_1): TR = 6.8–7.2, TE = 3.2 ms, TI = 900 ms, flip angle = 90, voxel size = $0.75 \times 0.75 \times 0.8$, acceleration factor 2 in slice direction, acquisition time = 7:02 min; 2) 3D T_2 weighted FSE (T_2): TR = 2500, TE = 225–245, voxel size = $1 \times 1 \times 2$ or $1 \times 1 \times 1$, acceleration factor 2 in slice and phase directions, acquisition time = 5:03 min; and 3) 3D FLAIR: TR = 4800, TE = 271–415, TI = 1600, voxel size = $0.9 \times 0.9 \times 1$, acceleration factor 2 in slice direction, 2.6 in phase direction, acquisition time = 6:10 min. All scans were acquired sagittally.

2.4. Image preprocessing

For each individual subject, T_2 and FLAIR images were co-registered to the T_1 with an affine transformation using a normalized mutual information cost function and resampled to the T_1 grid using AFNI. Registered images were visually assessed for alignment. Cortical reconstruction was performed using T_1 and T_2 images as input to FreeSurfer's standard processing pipeline with FreeSurfer v6.0.0 (Dale et al., 1999; Fischl et al., 1999). Results were visually inspected and manually corrected as needed. Cortical surfaces were resampled to a standard mesh using the AFNI SUMA package (Cox, 1996) to allow for comparison of corresponding vertices across individuals.

2.5. SNSNRSNR= SNR aware local image filters

Next, we constructed SNR-aware local image filters, used subsequently both to correct for MRI coil-induced variations in image intensity, and to compute local 3D multi-scale oriented filters that serve as the basis for our normative model of cortical variability. We implemented these SNR-aware filters to correct for the impact of the sharp boundary between the outer edge of the head and air (seeSupplementary Figure S1 for a comparison of Gaussian and SNR-aware image filters). These edge effects are a known issue for MRI coil inhomogeneity correction approaches that estimate the coil sensitivity profile as a blurred version of the image. Most current approaches address this issue by using a simultaneous segmentation and bias field estimation (Ganzetti et al., 2016). Here, instead of carrying out a full segmentation, we created an estimate of signal likelihood, borrowing from the computational neuroscience literature describing exponentiation (see review in (Carandini and Heeger, 2011)). Our signal likelihood estimate is based on the assumption that voxels with near zero intensity are most likely noise, while those with higher intensities, particularly those near or above the average signal intensity, are most likely signal. Signal likelihood can thus be modeled similarly to the output of a single neuron, or the positive half of a logistic function, which is an exponential function $(1 - e^{(-x/s)})$ that ranges between 0 and 1. This function has a single free parameter, the scale s, which is used to "tune" the curve, such that voxels with intensities above the estimated signal mean have high signal likelihood, with signal likelihood falling off exponentially with decreasing intensity below the mean (Supplementary Fig. 1 top and middle right). We then use these signal likelihood estimates to weight our filtered

images.

To create the signal likelihood estimates, we used a data-driven iterative process. First, we defined the signal likelihood $w_s(\vec{r})$, and the noise likelihood $w_n(\vec{r})$ for each location $\vec{r}$ in each 3D image heuristically as:

$$w_s(\vec{r}) = 1 - e^{-f(\vec{r})/\mu_s}$$
$$w_n(\vec{r}) = 1 - w_s(\vec{r}) = e^{-f(\vec{r})/\mu_s}$$

where $f(\vec{r})$ is the image intensity at location $\vec{r}$, and μ_s is the global signal mean for all voxels with non-zero signal. We defined the signal (μ_s) and noise (μ_n) means as weighted averages of the image intensity:

$$\mu_s = \frac{\sum_i w_s(\vec{r_i})f(\vec{r_i})}{\sum_i w_s(\vec{r_i})}, \mu_n = \frac{\sum_i w_n(\vec{r_i})f(\vec{r_i})}{\sum_i w_n(\vec{r_i})}$$

The signal and noise likelihoods at each location and the global signal and noise means were computed as follows:

1. initialize $w_s(\vec{r})$ to 1 for all non-zero voxels
2. iterate:
   – given $w_s(\vec{r})$, compute μ_s
   – given μ_s, compute $w_s(\vec{r})$
3. compute $w_n(\vec{r})$
4. compute μ_n.

Three iterations of step 2 were sufficient to achieve convergence of the signal likelihood to 3 digits.

We then used the signal likelihood function $w_s(\vec{r})$ and global signal μ_s and noise μ_n levels to construct SNR aware local image filters consisting of a set of K Gaussian derivative filters, denoting the kth filter's kernel by $G_k(\vec{r})$. We applied the kth filter to an image $f(\vec{r})$ in analogy to a local weighted average to obtain the kth filtered image $f_k(\vec{r})$:

$$f_k(\vec{r}) = \frac{G_k(\vec{r}) \otimes (f(\vec{r})w_s(\vec{r}))}{G_k(\vec{r}) \otimes w_s(\vec{r})}$$

Division in the above expression was regularized using a term proportional to the global signal to noise ratio:

$$\frac{1}{\phi(\vec{r})} \approx \frac{\phi(\vec{r})}{\beta^2 + \phi(\vec{r})^2}$$

$$\beta = 0.01 \frac{\mu_n}{\mu_s}$$

in order to prevent noise amplification in the estimate of $f_k(\vec{r})$ in regions of the image where the local signal likelihood $w_s(\vec{r})$ was very small, e.g. outside the head.

2.6. Local intensity correction

Intensity correction for each 3D image was carried out by dividing each image by an estimate of its local mean image intensity, computed by applying an SNR-weighted 3D Gaussian filter of width 64 mm (Supplementary Fig. 1 bottom). This filter width was selected as it appeared to provide correction of coil-induced inhomogeneities, as can be seen through the narrower distribution of intensities, compared to the raw image (Supplementary Fig. 2) while preserving some separation between gray and white matter intensities (see the two distinct peaks in Supplementary Fig. 2, level 5, corresponding to a filter width of 64 mm). The use of smaller radius filters leads to a narrower distribution of observed intensities at the cost of diminished distinction between gray and white matter voxel intensities.

2.7. Feature generation

To represent the characteristics of the local neighborhood surrounding each voxel in a manner that was insensitive to the local orientation of the cortical sheet, we created a set of rotationally invariant 3D multi-scale local image filters analogous to the multi-scale oriented filters that have been shown to be: 1) an efficient representation of natural image local statistics; 2) an accurate model of neurons in the mammalian visual system; and 3) a reliable model commonly used in computer vision applications to create a robust, efficient, generic basis set for applications such as texture synthesis (Simoncelli and Olshausen, 2001).

Using the SNR-weighted filters described above, for each image we computed zeroth, first, and second order derivatives of the Gaussian at three spatial scales (2, 4, and 8 times lower resolution or blurring):

- zeroth order: 1 image, scalar, $\{g\}$
- first order: 3 images, vector, $\{g_x, g_y, g_z\}$
- second order: 6 images, tensor, $\{g_{xx}, g_{xy}, g_{xz}, g_{yy}, g_{yz}, g_{zz}\}$

where g_x is the derivative of the gaussian in the x-direction, etc. At each spatial scale, we then combined the gradient filtered images to form rotationally invariant feature images. The zeroth order Gaussian blurred image is a scalar. The first order gradient images form a vector, and we consider only its magnitude. The second order gradient images form a symmetric tensor, and we consider only its trace (Laplacian of Gaussian) and magnitude of the Hessian, resulting in four images at each spatial scale:

$$G = g$$
$$M = \sqrt{g_x^2 + g_y^2 + g_z^2}$$
$$L = g_{yy} + g_{yy} + g_{zz}$$
$$H = \sqrt{g_{xx}^2 + 2g_{xy}^2 + 2g_{xz}^2 + g_{yy}^2 + g_{yz}^2 + g_{zz}^2}$$

This resulted in a 39 dimensional feature vector at each voxel (Fig. 1).

2.8. Prediction of typical features

Because these features theoretically represent an efficient and overcomplete representation of the local features of each image, we hypothesized that we should be able to predict the values of other commonly used local features such as curvature, sulcal depth, cortical thickness, and gray/white contrast (as calculated using FreeSurfer) or measures of myelination, here calculated by dividing the T_1 by the T_2 intensity, as in (Glasser and Essen, 2011), sampled onto the gray-white junction surface. Using scikit-learn, our feature set served as the input to ordinary least-squares regression models (polynomial order 2), predicting each target feature. We trained on the data from half of the HVs and tested on the other half.

2.9. Normative model generation

Next, we sought to create a normative model to represent the expected variability seen across the cortical sheet in healthy volunteers in our feature space (see overview in Fig. 2). This normative model provides an estimate of the probability distribution for each feature in this reference population. Individual patient data can be compared to this distribution, providing the basis for our constrained outlier detection approach to FCD identification. The typical MR findings of FCDs tend to be centered around the gray - white matter junction (GWJ), with characteristic alterations described in the signal intensity in the cortical gray matter and underlying white matter as well as GWJ blurring. Since our features are designed to represent the local neighborhood surrounding each voxel, we hypothesized that these characteristic FCD-related
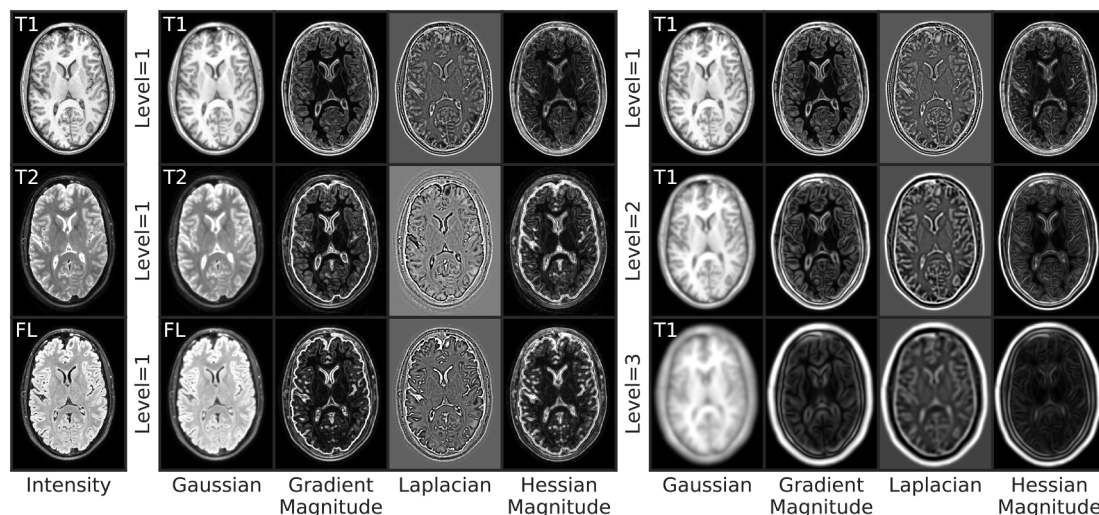
Fig. 1. Features. For each of the intensity-corrected T, T_2, and FLAIR images (left), four 3D rotationally-invariant derivative-based local image filters were computed, consisting of the Gaussian, magnitude of the gradient, Laplacian of Gaussian, and magnitude of the Hessian (middle). Each was computed at three spatial scales or levels (2, 4, and 8 times lower resolution), shown for the T_1 image contrast (right), resulting in a 39-feature vector for each voxel.
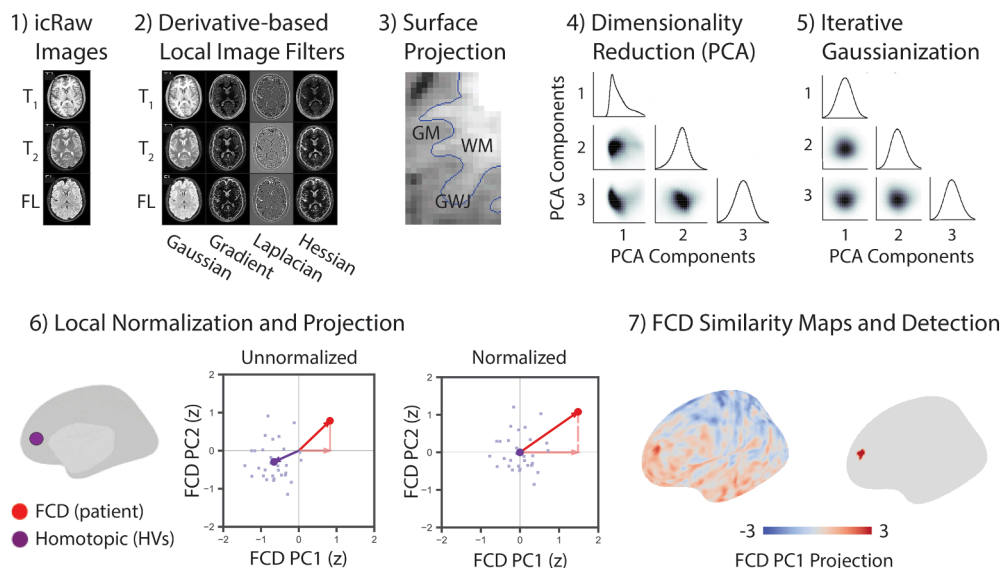

Fig. 2. Methods Overview. 1) Raw T_1, T_2, and FLAIR images were intensity corrected, 2) local image filters were computed in the volume then 3) sampled onto the gray-white junction surface; each feature was standardized within each subject. 4) Across healthy volunteers, dimensionality reduction was carried out using PCA, resulting in 14 features explaining 90% of the variance. 5) Iterative Gaussianization was used to non-linearly convert each feature to a multivariate Gaussian distribution, creating a normative model of cortical variability. 6) An average FCD vector was computed across all visually identifiable FCDs in our patient sample. Similarity to the average FCD vector was assessed by projecting each patch onto the average FCD unit vector. Local normalization was performed for each cortical location by subtracting the mean across homotopic patches in healthy volunteers at each location. The purple HV homotopic patches can be seen to become centered around 0 following local normalization, while the FCD location becomes more atypical along both the FCD PC1 and PC2 directions. 7) Similarity maps were created based on the projection onto the mean FCD unit vector at each cortical location. These maps were thresholded at 1%, retaining clusters of > 5 vertices. An optimal threshold was defined using mean similarity across each remaining cluster to distinguish between true positive FCD clusters and false positive clusters in healthy volunteers. Clusters above this threshold are detected as FCDs. (For interpretation of the references to color in this figure legend, the reader is referred to the web version of this article.)

abnormalities could be sufficiently identified by multiscale local image filters centered on the voxels at the GWJ. Additionally, other approaches have successfully utilized surface-based approaches to FCD detection (such as in (Hong et al., 2014; Jin et al., 2018; Adler, 2017a; 2017b;; Ahmed et al., 2015; Thesen et al., 2011)). We therefore sampled our 39 feature vector onto the FreeSurfer generated smooth white matter surface. Each feature was standardized within each subject. This was followed by dimensionality reduction and whitening using principal component analysis (PCA) of all cortical vertices across all HVs implemented in scikit-learn in Python (Pedregosa et al., 2011), retaining 14 components explaining 90% of the variance.

Next, in order to facilitate more straightforward multivariate outlier detection, we implemented a rotation-based iterative Gaussianization (RBIG) procedure to transform the data into a latent representation with a known probability density function (PDF), in this case a multivariate Gaussian distribution (Fig. 2) (Laparra et al., 2011). This is a form of representation learning similar to an auto-encoder, in which the data undergoes a nonlinear transformation for the purposes of facilitating more straightforward statistical inferences (Bengio et al., 2013). Amongst the many available methods such as other types of autoencoders or deep learning methods, we elected to use RBIG specifically to facilitate multidimensional outlier detection based on deviation from the expected values in the healthy population. The RBIG procedure consists of 10 iterations of a pair of sequential transformations: 1) a nonlinear univariate Gaussianization transformation applied to each of the data matrix columns (marginals) that converts percentile scores computed using the rank transformation to standard scores (scikit-learn's QuantileTransformer); and 2) a linear orthogonal transformation applied to the entire data matrix using PCA, retaining all components after each iteration (Laparra et al., 2011). Source code for generating the features and model is publicly available on GitHub as part of the JEM python package (http://github.com/InatiLab/jem).

2.10. Outlier detection

Using our normative model of cortical variability, we wished to identify whether vertices within FCD lesions appeared as global outliers compared to non-lesional vertices in healthy volunteers. To smooth the data and facilitate comparisons across subjects, we created patches centered at every vertex, including all neighboring vertices within a 5 mm radius, and used this smoothed data for all subsequent analyses. This radius was selected to be small enough to identify changes within specific gyri/sulci, and large enough to minimize local noise and artifacts, and is similar to the smoothing size used in similar studies, for example (Adler et al., 2017a; 2017b). For each patch p, the center $\mathbf{m}_p$ was computed by averaging the feature vectors of the vertices within the patch: $\mathbf{m}_p = \sum_{\mathbf{x} \in p} \mathbf{f}(\mathbf{x})$. The direction $\hat{u}_p$, the unit vector pointing in the direction of the patch's center, was computed by dividing the patch's mean feature vector by its length $\hat{u}_p = \mathbf{m}_p / \|\mathbf{m}_p\|$. For each normal or pathological ROI, we defined the center and direction as the average across patches within that ROI. To create an average FCD vector, we computed the average across patches within each MRI+ patient's FCD mask (n = 11), then averaged across patients to give each lesion equal weighting regardless of size.

In our feature space, outliers can be defined by the Mahalanobis distance, MD, or the distance from the origin to the patch's center, as the probability of finding a patch with a given average feature vector $\mathbf{m}_p$ depends only on the magnitude of the feature vector $\|\mathbf{m}_p\|$ and not on its direction, with MD^2 following a cumulative chi-squared distribution. Across healthy volunteers, we explored whether some normal cortical regions appeared as outliers in our model. We arbitrarily defined patches with an average distance from the center (MD) of > 2.7 as outliers, corresponding to the top $\sim 5\%$ of patches (p = 0.043). We retained all resulting clusters with > 30 vertices in order to eliminate isolated atypical patches, as we were seeking to identify outlier regions

at larger spatial scales as described by studies of cortical cyto- and myeloarchitecture. Of the resulting clusters, we selected two of the three most outlying regions of interest (ROI) as exemplars (insula and precentral regions). We then explored to what extent FCD patches were outliers in our feature space. We measured the Mahalanobis distance (MD) of 1000 randomly sampled patches from randomly sampled normal cortex across HVs and 1000 patches selected from FCD lesion masks in patients and compared these to our normal cortex exemplar outlier regions.

2.11. Similarity estimation

Having observed significant overlap in outlierness between FCDs and some normal cortical regions, we explored the similarity in underlying features between FCDs and normal cortex. To assess similarity between cortical patches p_i and p_j without regard to degree of outlierness, we assessed the angle between their feature vectors, as well as the cosine similarity between their directions $s_{ij} = \hat{u}_i \cdot \hat{u}_j$. Using these metrics, patches with similar relative combinations of underlying features will have a smaller angle between them and will appear more similar regardless of their distance from the center of the distribution. We first wished to explore the similarity between our outlier ROIs and FCDs. To aid with visualization, we plotted the mean feature vectors for the insula, precentral, and FCD ROIs in 2D using the insula and precentral ROI directions as axes, then using the first two FCD PCA components as axes. We also measured the angles between the mean FCD vector and the mean vectors of the normal cortical outlier regions. In a related approach, we created similarity maps for each outlier ROIs and for FCDs by computing the scalar projection of the mean feature vector for each cortical patch onto the ROI average unit vector and projecting it onto the cortical surface (see Fig. 2). This metric identifies cortical regions that are outliers with similar underlying features to the exemplar ROI.

Lastly, based on known patterns of cortical variability, we hypothesized that local image features would vary across the cortical sheet in a somewhat reproducible fashion across HVs and therefore patches in the same locations would appear more similar to each other than patches in different locations. We defined patches as being in homotopic (same) or heterotopic (different) locations as defined by the standard surface mesh and computed the cosine similarity between 1000 randomly sampled heterotopic patches and 1000 homotopic patches across HVs. To determine how similar FCD lesions appeared to normal cortex, we then compared the cosine similarity of 1000 non-overlapping FCD patches to each other, as well as to 1000 randomly selected heterotopic and then homotopic patches across HVs.

2.12. Local normalization

Because FCDs were not more globally anomalous and also appeared to have similar features to some normal cortical regions, we hypothesized that to be identifiable, FCDs must differ from the expected appearance at their underlying location, or homotopic region, in HVs. We implemented a local normalization procedure by removing the local mean, calculated across homotopic patches in HVs. We expected that after local normalization, reproducible regional differences in normal cortex should no longer be present. However, the effect on FCDs was unknown. Therefore, following normalization, we again compared the Mahalanobis distances of normal cortex, the outlier ROIs, and FCDs as above, as well as the cosine similarity between FCD patches and heterotopic and homotopic normal cortical patches.

2.13. Automated FCD detection

We created an automated FCD detection method based on locally normalized FCD similarity maps. We used a leave-one-out cross-validation strategy to build a subject specific model for each FCD patient

and HV. In each subject, we computed the scalar projection of the mean feature vector for each patch onto the FCD average unit vector (Fig. 2). We then applied a threshold to identify the top 1% of vertices and retained clusters with 5 or more adjacent remaining vertices, a minimal size threshold meant to eliminate isolated outlying vertices. For each surviving cluster, we computed the mean FCD similarity.

2.14. Statistical analysis

All statistical analyses were carried out in Python. For the feature prediction models, performance was evaluated for each model using the coefficient of determination r^2. To estimate the extent of the differences between the measured and predicted models, we report effect size as in (Cohen, 1988): $r = 0.1$ as *small;* $r = 0.3$ as *medium;* and $r = 0.5$ as *large.* For distance-wise comparisons between patches, we used Welch's un-equal variance *t*-test to assess significance and to estimate the effect size of the differences, reported as in (Cohen, 1988): $d = 0.2$ as *small;* $d = 0.5$ as *medium;* and $d = 0.5$ as *large.*

Sensitivity of the automated FCD detection procedure was assessed initially for MRI+ patients and then for all patients. We calculated a receiver operating characteristics (ROC) curve and area under the curve (AUC) based on the patients with manual lesion labels that were included in the leave-one-out analysis. True positives were defined as co-localization of a detected cluster with the manual lesion mask for MRI+ patients and as overlap of a detected cluster with the resection mask for MRI- patients. False positives were defined as HVs with clusters detected above a given threshold. The optimal threshold for the final detection was determined using the Youden Index (calculated as sensitivity+ specificity − 1 for each threshold) in the patients with lesion masks. Lesion detection and number of extralesional clusters (outside of the lesion and resection masks or in HVs) were assessed for all patients and HVs individually.

3. Results

3.1. Study participants

This study includes 15 patients with drug resistant focal epilepsy and FCD (median age 27, range 15–53, 11 females) and 30 healthy controls (median age 23, range 8–63, 12 females). FCDs were identified in the radiological reports in 6/15 patients; an additional five patients had lesions identifiable on post-hoc analysis (MRI+ n = 11) (details in Table 1 Patient Demographics).

3.2. Feature prediction

To evaluate whether our 14-dimensional Gaussianized local image filter feature set encompasses information captured using more typically utilized local features, we trained quadratic regression models to predict several typical features (Fig. 3). Predictions were accurate with large effect sizes for FreeSurfer measures of curvature and sulcal depth ($r^2 = 0.80$ and $r^2 = 0.73$ respectively), gray-white contrast ($r^2 = 0.61$), and cortical thickness ($r^2 = 0.46$), as well as myelin contrast ($r^2 = 0.39$). Spatial distributions appear similar between measured and predicted features when mapped onto the cortical surface.

3.3. Outlier detection

In our normative model, outliers can be identified based on their distance from the center of the distribution (Mahalanobis distance (MD)). Across HVs, we identified twelve and seven consistent outlier regions in the left and right hemispheres respectively, located mostly in or adjacent to primary sensorimotor cortices or in limbic and paralimbic regions (Fig. 4a). We selected two of the top three outlier regions as exemplar ROIs, located in the anterior insula and precentral gyrus (Fig. 4b). FCDs were significant outliers compared to randomly selected cortical patches (FCD MD = 3.53 ± 0.60 versus random patches MD = 2.61 ± 0.57, p < 0.001, $d = 1.60$), but only to a similar extent as these normal outlier regions (precentral MD = 3.46 ± 0.43, $d = 0.16$, insula MD=3.36 ± 0.36, $d = 0.41$).

3.4. Similarity estimation

Next, we assessed the similarity in underlying features, or directions, between FCDs and the normally outlying cortical regions. The average angle between the mean FCD and outlier region centers was $81.01 \pm 23.30^{\circ}$ (minimum: 38.56° in the anterior parahippocampal gyrus, maximum: 123.16° in the post-central gyrus). The insula was second closest in angle (42.2°), while the precentral ROI was close to the average difference (80.3°) (Fig. 4b). This is reflected in the similar spatial distributions of the insula and FCD similarity maps, which clearly differ from that of the precentral similarity map (Fig. 4c). This suggests that FCDs appear similar in both degree of outlierness and underlying features to some atypical regions of normal cortex, such as the anterior insula and some paralimbic regions.

Next, we used cosine similarity (cos) to describe how similar patches are to each other in their underlying relative combination of features
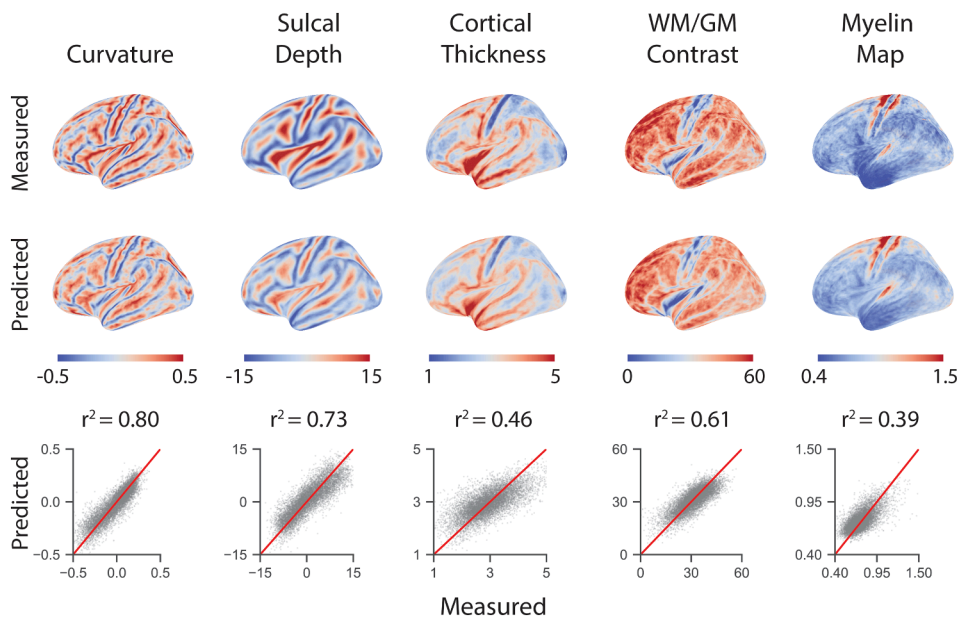
Table 1
Patient Demographics.

Patient #	Sex	Age	Seizure onset	Epilepsy duration	Lesion lobe	Lesion Resection	Seizure Outcome	Pathological Diagnosis	MRI
1	F	33	1	32	RF	Y	1a	FCD IIb	+
2	F	40	3	37	LC	–	–	transmantle	+
3	F	53	12	41	RC	–	–	transmantle	+
4	F	21	3	18	RP	–	–	transmantle	+
5	F	25	22	3	LF	–	–	–	+
6	F	17	11	6	RT	–	–	transmantle	+
7	F	43	8	35	RF	Partial	3a	FCD IIb	–
8	F	40	6	34	LF	–	–	–	–
9	F	47	20	27	RP	–	–	–*	–
10	M	37	19	18	LT	–	–	–*	–
11	F	21	3	18	LF	Y	1a	FCD IIa	–
12	M	27	9	18	RP	Y	1a	FCD IIa	–
13	M	26	7	19	LF	Y	1a	FCD IIb	–
14	M	15	3	12	RF	Partial	3	FCD IIa	–
15	F	22	21	1	LC	Partial	4	FCD IIa	–

Age and epilepsy duration are reported in years at the time of the scan. Lesion resections are reported as yes (Y) if they were thought to be complete lesionectomies at the time of surgery; resections were partial (part) if they were limited by overlap with functional cortex. Seizure outcome is reported as Engel Class at 12 months. Transmantle signs were listed if no pathological evaluation was available, as these are thought to be present primarily in FCD type IIb lesions. Lesion lobe abbreviations: R = right, L = left, F = frontal, C = central, P = parietal, T = temporal. *patients who did not undergo resection (Pt 8) or sufficient pathologic examination of the tissue of interest (Pt 9) but were found to have electrographic correlate with the relevant imaging finding on invasive EEG recordings.

Fig. 3. Feature Prediction. We were able to predict several commonly used cortical features using our 14 normalized multivariate Gaussian features from our HVs as inputs into quadratic regression models. The top row displays the spatial distribution of the measured values of each feature; the middle row displays the predicted features from our models, averaged across HVs plotted on the cortical surface; cool-warm color scale is used to highlight the spatial consistency of the extrema for each measure. Measured versus predicted values for each cortical patch are plotted against each other (bottom); coefficients of determination (r^2) are reported for each.
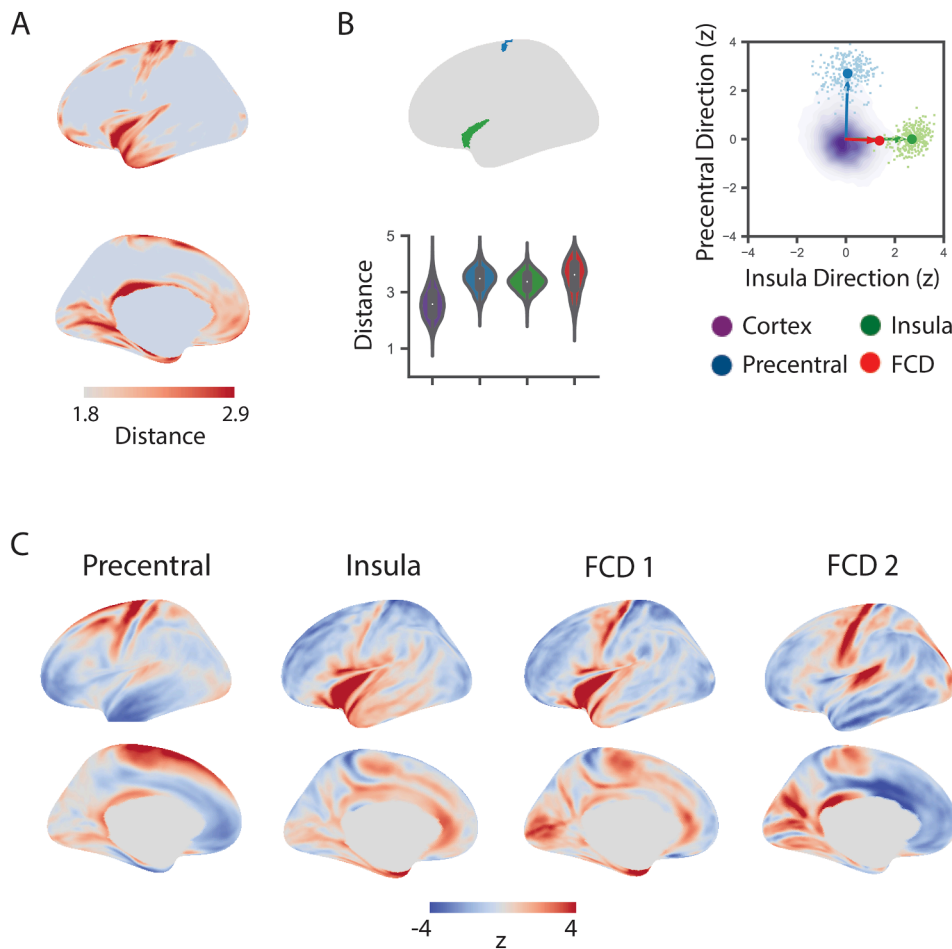

Fig. 4. FCD Comparison to Normal Cortical Outlier Regions. (A) Mahalanobis distances (from the center) of each cortical patch averaged across 30 HVs is plotted onto the smoothed cortical surface, highlighting the variability across the cortex. (B) Left: The top ~ 5% of outlier patches in HVs were selected and clustered; two exemplar ROIs were selected in the anterior insula (green) and precentral regions (blue). Patches from the two exemplar ROIs as well as from FCDs are global outliers compared to randomly selected cortical patches (purple). Right: The locations of patches within these two ROIs across HVs and the average FCD center (red) is plotted in 2D using the primary directions of the centers (larger dots) of each exemplar ROI as the axes. (C) Similarity maps are shown for each of our exemplar normal cortical outlier ROIs, as well as for the first two components of the average across FCDs. (For interpretation of the references to color in this figure legend, the reader is referred to the web version of this article.)

based on their location (Fig. 5a). We found that across HVs, homotopic patches (in the same location on the cortical sheet) appeared more similar than randomly selected patches ($cos = 0.45 \pm 0.28$ for homotopic versus $cos = 0.00 \pm 0.29$ for heterotopic random patches, $p < 0.001$, $d = 1.57$). Despite their differing locations, FCD patches were more similar to each other in their features ($cos = 0.29 \pm 0.29$) than to random HV cortical patches (FCD vs heterotopic patches $cos = 0.006 \pm 0.29$, $p < 0.001$, $d = 0.97$), and also appeared quite similar to homotopic patches in HVs (FCD vs homotopic patches $cos = 0.24 \pm 0.31$, $p = 1.78$, $d = 0.17$), consistent with the fact that these
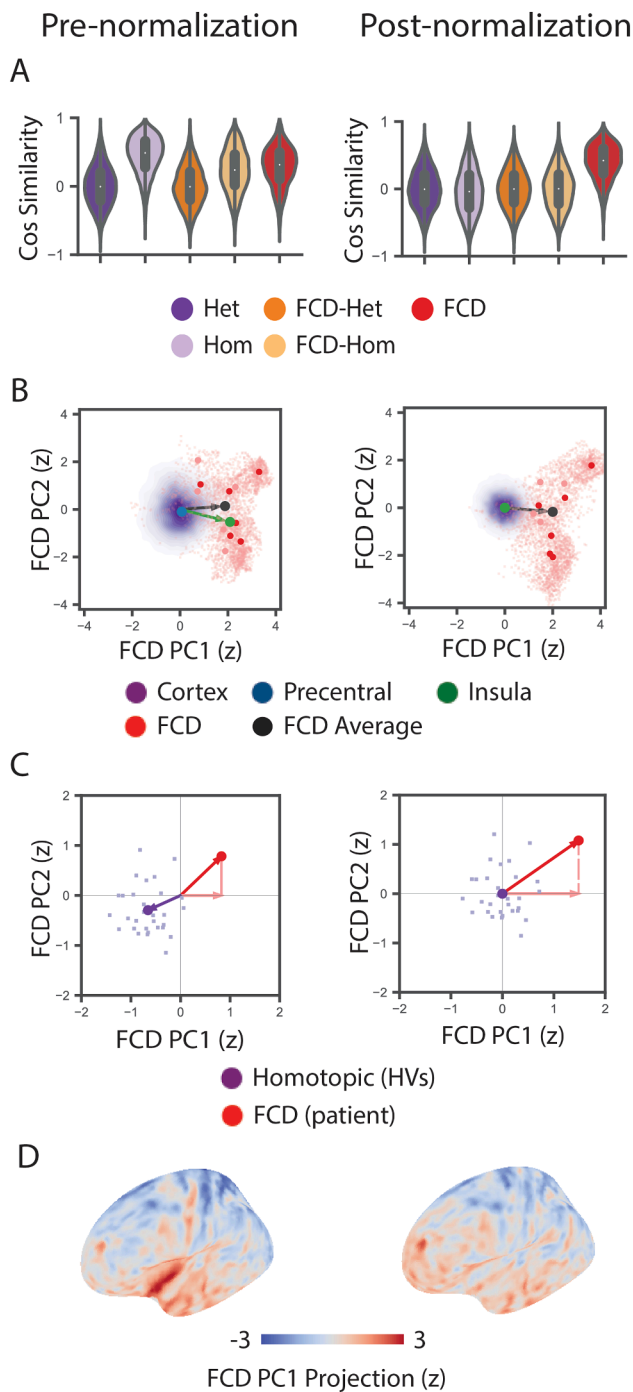
Fig. 5. Local Normalization: (A) (Left) Prior to local normalization, 1000 pairs of patches in homotopic (hom) cortical locations across HVs have increased cosine similarity compared to 1000 pairs of randomly selected heterotopic (het) patches. Patches across FCD lesions (1000 pairs) (FCD) also have increased cosine similarity compared to randomly selected heterotopic patches in HVs. FCD patches and homotopic patches are more similar to each other than to randomly selected patches in HVs (FCD-Het vs FCD-Hom). Following local normalization, cosine similarity between pairs of homotopic and heterotopic patches in HVs, as well as between FCD patches and HV patches in any location are similar and are centered around 0, while cosine similarity between FCD patches remains elevated. (B) Using the first two SVD components from the FCD patches as the axes, we plotted the location of: 1) each FCD patch (light red small dots); 2) the center of each individual FCD lesion (larger dots: MRI+ dark red, MRI- light red); and 3) the overall average FCD center across all subjects (black) compared to the insular ROI center (green), precentral ROI center (blue), and 1000 randomly sampled HV patches (purple). Following local normalization, the distribution of random cortical patches can be seen to become smaller, the insula and premotor ROI centers move to the center, and the FCD patches remain as outliers. (C) The mean feature vector for a single exemplar FCD lesion (red) is plotted along with homotopic patches in 30 HVs (purple). FCD similarity is measured by projecting each patch onto the FCD unit vector (light red arrow). The same exemplar FCD and its homotopic patches are shown after local normalization; the homotopic patches become centered around the origin and the FCD vector moves farther from the center, with a higher value when projected onto the mean FCD direction. (D) FCD similarity map is shown for the patient in (C). The frontal lesion appears similar before and after local normalization, while outlying regions such as the anterior insula no longer appear similar after local normalization. (For interpretation of the references to color in this figure legend, the reader is referred to the web version of this article.)

often subtle lesions have a fairly typical appearance for their given location.

3.5. Local normalization

While FCDs can be found in nearly any cortical region, normal cortical outlier regions by definition have fairly consistent spatial locations across HVs. Local normalization allows for detection of differences from the expected appearance at any given cortical location. Following local normalization, as expected, we found that patches in the outlier ROIs appeared more "typical" for their location, now with a similar Mahalanobis distance to randomly selected cortical patches (random cortex MD $= 1.86 \pm 0.52$ versus precentral MD $= 1.92 \pm 0.52$, $d = 0.10$, and insula MD $= 1.59 \pm 0.36$, $d = 0.63$). In contrast, following local normalization, FCDs remained as significant outliers (MD $= 3.55 \pm 0.81$) compared to both normal cortex and the previously outlying ROIs (versus normal cortex $d = 2.81$, precentral $d = 2.78$, insula $d = 4.09$). Cosine similarity between FCD patches also became significantly higher following local normalization (0.40 ± 0.26) compared to non-lesional patches at any location (to homotopic patches $cos = 0.00 \pm 0.30$, $p < 0.001$, $d = 1.40$, and to heterotopic patches $cos = 0.00 \pm 0.28$, $p < 0.001$, $d = 1.44$, with no difference between the two, $p = 0.54$) (Fig. 5a). Local normalization, therefore, not only aids with global outlier detection by decreasing the outlierness of normal cortical regions, but also local outlier detection, by further distancing FCDs from the expected appearance at their location in the cortical sheet.

3.6. Automated FCD detection

Our automated FCD detection method is based on the post-normalization FCD similarity maps, in which the mean feature vector for every cortical patch is projected onto the FCD average unit vector (Fig. 5c and d). The top 1% of patches were identified in each subject; clusters with five or more adjacent remaining vertices were retained. The final detection threshold was selected based on the optimal trade-off between sensitivity and specificity. We initially evaluated the 11 MRI+ patients (five initially MRI-) included in the leave-one-out analysis, resulting in an AUC of 0.91. At the optimal threshold determined from this analysis, our classifier correctly identified the lesions in 11/11 MRI+ patients (100% sensitivity) and 12/15 patients overall (80% sensitivity), yielding an eventual AUC of 0.96. Of the three patients

without detected lesions, one had a true positive (TP) lesion that did not reach the threshold; the others had no detected clusters that overlapped with their resection masks. Of 13 patients with TP clusters, the known FCD had the highest mean cluster weight in 11, with 1–3 clusters detected in each patient. One to three presumably false positive clusters were identified in 9/30 HVs (70% specificity). Table 2 summarizes the results individually for each patient; data for two exemplar patients are shown in Fig. 6.

To evaluate the effects of some model parameters on the accuracy of our automated detection, we found that adding or subtracting spatial scales did impact the performance. Using only two spatial scales for the underlying filters yielded an AUC of 0.77, while utilizing four spatial scales yielded an AUC of 0.85. Using the full set of 39 features versus the 14 features obtained that explained 90% of the variance showed minimal effect on performance, with an AUC of 0.9 versus 0.96, respectively.

4. Discussion

We used a novel normative modeling approach to compare local features of FCDs to those of normal cortex. We found that FCDs on average are global outliers but not more so than some atypical regions of normal cortex. In addition, the features seen in FCDs appear quite similar to those found in some outlying cortical regions such as the anterior insula and paralimbic cortices. After locally correcting for the expected appearance at each cortical location, FCD lesions become more easily distinguishable from normal cortex, with true positive clusters found in 13/15 patients, with 12/15 lesions detected at the optimal threshold, allowing for automated detection with 80% sensitivity and 70% specificity and an AUC of 0.96.

The performance of any FCD detection method depends on the features used to create an effective representation of the data. Here, we implemented a generic set of multiscale 3D rotationally-invariant derivative-based filters applied to T_1, T_2, and FLAIR images. Similar 2D filters have been used in computer vision applications such as texture synthesis and imaging denoising (Portilla et al., 2003) and occasionally in biomedical applications such as brain tumor classification (Zacharaki et al., 2009), lung disease segmentation (Joyseree et al., 2018; Wang et al., 2018) and cerebral white matter lesion detection (Selvaganesan et al., 2019). Most post-processing approaches to FCD detection to date have used features derived from voxel-based or surface-based morphometry (see review in (Kini et al., 2016)), including a variety of measures of image intensity and blurring of the gray-white junction,

Table 2
Patient Results.

Patient #	Lesion lobe	Pathological diagnosis	Radiology	Post-hoc	Detection	TP Mean	TP Rank
1	RF	FCD IIb	+	+	+	2.41	1 / 2
2	LC	transmantle	+	+	+	2.12	1 / 1
3	RC	transmantle	+	+	+	1.97	1 / 2
4	RP	transmantle	+	+	+	1.87	1 / 3
5	LF	–	+	+	+	1.78	1 / 2
6	RT	transmantle	+	+	+	1.69	3 / 3
7	RF	FCD IIb	–	+	+	2.26	1 / 1
8	LF	–	–	+	+	2.05	1 / 1
9	RP	-*	–	+	+	1.85	1 / 1
10	LT	-*	–	+	+	1.73	1 / 1
11	LF	FCD IIa	–	+	+	1.73	2 / 2
12	RP	FCD IIa	–	–	+	1.91	1 / 1
13	LF	FCD IIb	–	–	–	1.6	1 / 1
14	LC	FCD IIa	–	–	–	–	- / 3
15	RF	FCD IIa	–	–	–	–	- / 1

Lesion lobe and pathological diagnosis are repeated as in Table 1. MRI detection by visual inspection is reported both according to the initial radiological report and by retrospective evaluation based on other imaging and invasive recording results. Automated detection was positive (+) if the mean FCD likelihood across patches in the cluster was above the identified optimal threshold. Mean FCD similarity is reported for each true positive cluster. For each patient, the rank of each true positive cluster is reported (based on the cluster's mean FCD similarity), as well as the total number of clusters detected above the optimal threshold.
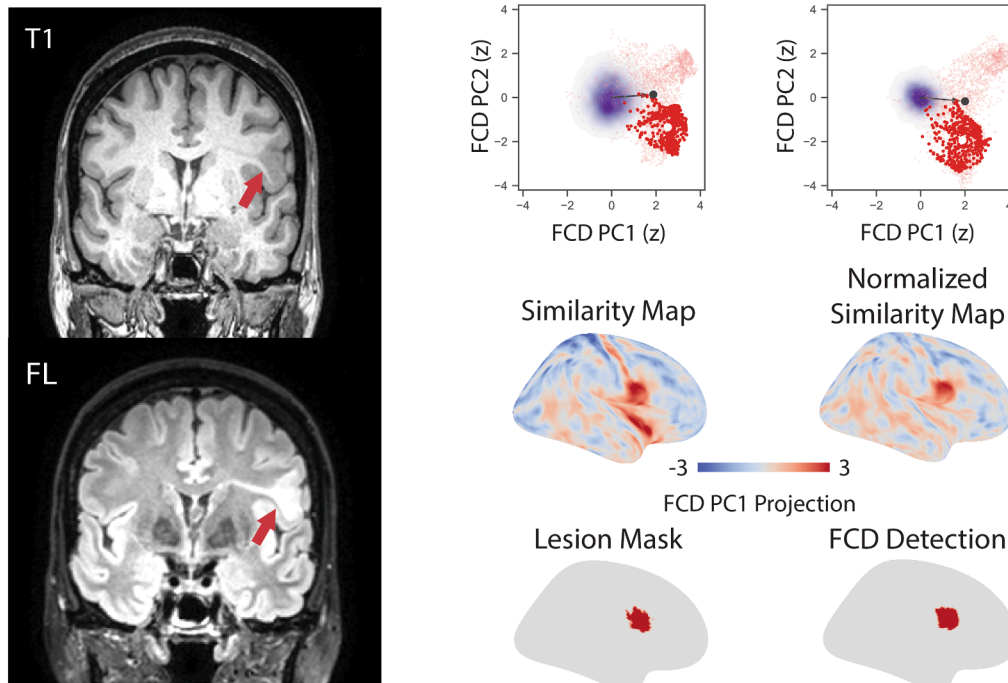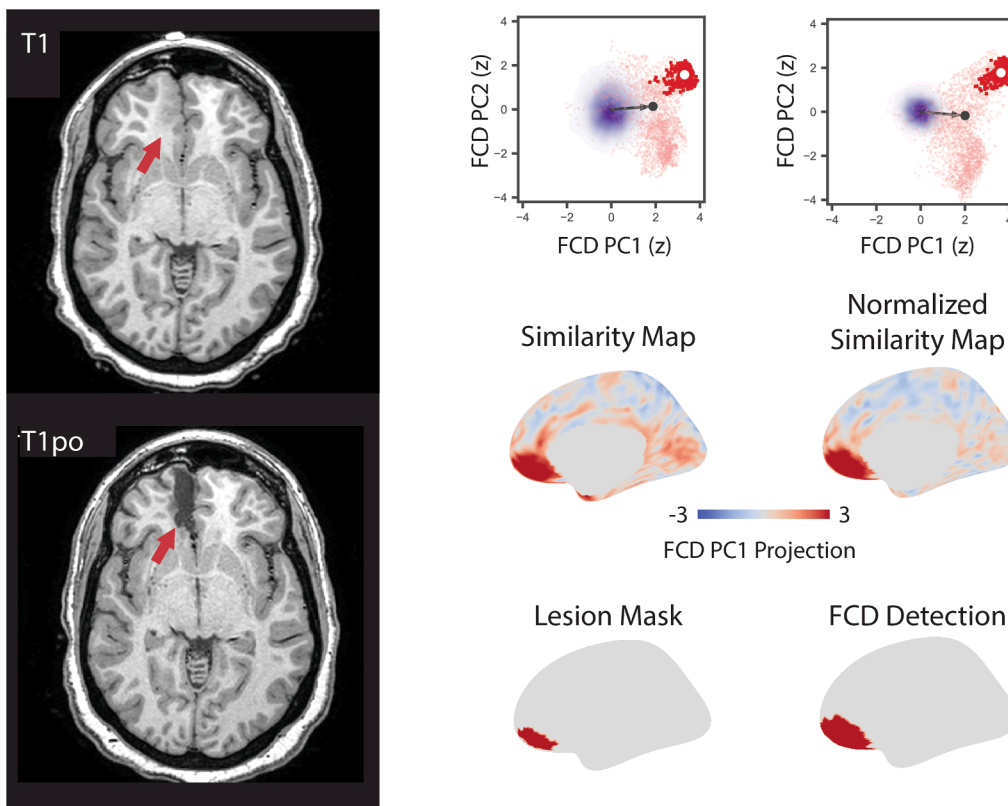
Fig. 6. Individual Patient Examples. Results for two exemplar patients: structural MRI (FL: FLAIR image, T1po: post-operative T_1) (left), location of FCD patches before and after local normalization (average vector for that patient's lesion: larger white dot and red arrow, patches within that patient's lesion: brighter red, patches from other FCD lesions: light red, randomly selected normal cortical patches: purple) (top right), FCD similarity maps before and after local normalization (middle right), and manually drawn lesion mask and automated FCD detection results (bottom right).

similar to our Gaussian blurring and gradient amplitude metrics. The filters that we have employed contain information similar to the higher-order textural features implemented by Antel et al., who used gray-level co-occurrence matrices derived from T_1-weighted images at a single spatial scale (Antel et al., 2003). Our features extend this work by additionally containing information from multiple spatial scales, as well as multiple MR contrasts. In our evaluation, we found that these features can be used to accurately predict other more commonly described features such as cortical thickness and myelination, as well as the FreeSurfer-defined metric of blurring of the gray-white junction, suggesting that they do encompass much of this local information.

Detection of subtle cortical lesions is challenging, at least in part due to difficulties in accounting for the variability of both the cortex and the lesions. Our normative model creates a single overall probabilistic representation of normal cortical variability that encompasses information from multiple local imaging features, spatial scales, and MR contrasts. We found that while FCD lesions are on average global outliers in appearance compared to normal cortex as a whole, some normal regions are outliers to a similar degree. FCDs also appear similar in their underlying average features to some of these normally outlying regions; the first component appears similar to regions such as the anterior insula and mesial temporal cortex, the second appears similar to sensorimotor and posterior cingulate cortices. These outlying regions generally consist of relatively thick agranular or dysgranular cortex (Amunts and Zilles, 2015; Triarhou, 2007; Zilles and Amunts, 2010) with relatively blurry gray-white junctions. However, they are at opposite ends of the known gradients in myelination; primary sensorimotor regions are heavily myelinated while paralimbic cingulate and parahippocampal cortices are lightly myelinated (Glasser and Van, 2011; Nieuwenhuys and Broere, 2017; Paquola et al., 2019). Accordingly, the precentral ROI similarity map parallels the myelination gradients, extending primarily toward the premotor regions, while the insula similarity map identifies the lightly myelinated, relatively thick anterior cingulate and parahippocampal cortices. Commonalities with the FCD similarity maps are likely attributable to these shared features.

Local normalization corrects for the expected appearance of the cortex in a given location, thereby allowing FCDs to be more easily distinguished from other normally outlying cortical regions. Interestingly, we observed that FCDs initially share some common features with their underlying homotopic cortical regions, with cosine similarities between FCDs and their respective homotopic regions being equal to that of other FCDs and significantly more similar than to random cortical areas. This finding is consistent with the fact that many of these lesions differ only subtly from surrounding cortex, which makes them difficult to appreciate visually. This is no longer seen following local normalization.

Our automated detection procedure based on these locally normalized FCD similarity maps allows for detection of 80% of FCDs and 100% of visually identifiable FCDs with 70% specificity. In patients with true positive clusters, the lesion of interest had the highest cluster weight in 11/13 (85%), thus providing an additional way of identifying lesions of higher interest in a given patient, similar to the approach used in Adler et al. (Adler et al., 2017a; 2017b). Many are also clearly identifiable by visual inspection of the FCD similarity maps, which can be reviewed similarly to the maps created using the MAP procedure (Wang et al., 2015; Wagner et al., 2011). The performance of our automated classifier is similar to previously reported machine learning methods, which have achieved 58–74% sensitivity, with specificities ranging from not reported to 100% (Adler et al., 2017a; 2017b;; Ahmed et al., 2015; Hong et al., 2014; Jin et al., 2018). Numerous factors may affect the performance of these methods, including alterations in model parameters, conspicuity of lesions studied (MR+ versus MR- patients), and size of the patient and healthy volunteer training sets utilized. For supervised machine-learning methods, performance appears to improve significantly with increasing size of the healthy volunteer and patient training sets (as in Jin et al., 2018, from 24 to 74 healthy volunteers, and 11 to 34

FCD patients), likely through improving modeling of both pathological and normal cortical variability.

Direct comparisons of performance across methods continues to be challenging, and to our knowledge, no work to date has directly compared the performance of different automated FCD methods in the same patient population. There are several challenges to adopting these techniques across centers, for research or for clinical use, including: 1) MR scanning protocol variability, hardware, and software, which may impair generalization of any "learning" across centers; 2) limited availability of large patient and normative training sets at single institutions, particularly with ongoing evolution of acquisition protocols; and 3) significant technical expertise required to implement these approaches. Our work, like others, is limited by the relatively small size of normative and lesional training sets. In the future, we hope to carry out a clinical validation in a larger group of patients, and to adopt other approaches to validation that may allow for more rigorous evaluation of performance compared to our leave-one-out evaluation approach. Open source efforts such as this and the MELD Project (https://meldproject.github.io/) will hopefully continue to increase adoption, allow for direct comparisons of methods, and allow for pooling of data across centers leading to improved performance (Jin et al., 2018).

Despite these limitations, our current findings do offer some novel insights. Our findings that some normal cortical regions are outliers, and that some of these regions have similar underlying features to FCDs, may explain the lack of specificity of many classification methods. The spatial reproducibility of these normal outlier regions also helps to explain why local normalization procedures improve the performance of many FCD detection methods. Finally, our 2D projections of FCD patches highlight the variable appearance of these lesions, again shedding light on why increasing the number of training lesions would improve the sensitivity of machine-learning based classification procedures and help to avoid overfitting.

5. Conclusions

We implemented a novel normative modeling approach to FCD identification, providing a robust characterization of normal cortical variability for comparison with FCD lesions. In keeping with their often subtle appearance, FCD lesions are outliers but only to a similar degree as some normal cortical regions. In our feature space, FCDs appear quite similar to some of these regions, such as paralimbic and anterior insular cortices. These similarities should be kept in mind when visually inspecting images to detect possible FCDs. They also help to explain the utility of local normalization procedures in reducing false positive detections. Our resulting approach to automated FCD detection is 80% sensitive and 70% specific, with an AUC of 0.96, similar to or better than many previously proposed methods, despite the relatively small size of the training and testing data. Our normative modeling approach also has the potential to be of use in the detection of other types of pathology or to study normal cortical variability.

CRediT authorship contribution statement

Kathryn Snyder: Methodology, Software, Formal analysis, Investigation, Writing - original draft, Visualization. **Emily P. Whitehead:** Software, Investigation. **William H. Theodore:** Resources, Writing - review & editing. **Kareem A. Zaghloul:** Resources, Writing - review & editing. **Souheil J. Inati:** Methodology, Software, Formal analysis, Writing - review & editing. **Sara K. Inati:** Conceptualization, Methodology, Resources, Writing - original draft, Supervision.

Acknowledgements

Appendix A. Supplementary data

Supplementary data to this article can be found online at https://doi.org/10.1016/j.nicl.2021.102565.

References

Adler, S., Lorio, S., Jacques, T.S., Benova, B., Gunny, R., Cross, J.H., Baldeweg, T., Carmichael, D.W., 2017a. Towards in vivo focal cortical dysplasia phenotyping using quantitative MRI. Neuroimage Clin. 15, 95–105.

Adler, S., Wagstyl, K., Gunny, R., Ronan, L., Carmichael, D., Cross, J.H., Fletcher, P.C., Baldeweg, T., 2017b. Novel surface features for automated detection of focal cortical dysplasias in paediatric epilepsy. Neuroimage Clin. 14, 18–27.

Ahmed, B., Brodley, C.E., Blackmon, K.E., Kuznieckyi, R., Barash, G., Carlson, C., Quinn, B.T., Doyle, W., French, J., Devinsky, O., Thesen, T., 2015. Cortical feature analysis and machine learning improves detection of MRI-negative focal cortical dysplasia. Epilepsy Behav. 48, 21–28.

Amunts, K., Zilles, K., 2015. Architectonic Mapping of the Human Brain beyond Brodmann. Neuron 88, 1086–1107.

Antel, S.B., Collins, D.L., Bernasconi, N., Andermann, F., Shinghal, R., Kearney, R.E., Arnold, D.L., Bernasconi, A., 2003. Automated detection of focal cortical dysplasia lesions using computational models of their MRI characteristics and texture analysis. Neuroimage 19, 1748–1759.

Bengio, Y., Courville, A., Vincent, P., 2013. Representation learning: a review and new perspectives. IEEE Trans. Pattern Anal. Mach. Intell. 35, 1798–1828.

Bernasconi, A., Antel, S.B., Collins, D.L., Bernasconi, N., Olivier, A., Dubeau, F., Pike, G. B., Andermann, F., Arnold, D.L., 2001. Texture analysis and morphological processing of magnetic resonance imaging assist detection of focal cortical dysplasia in extra-temporal partial epilepsy. Ann. Neurol. 49, 770–775.

Besson, P., Andermann, F., Dubeau, F., Bernasconi, A., 2008. Small focal cortical dysplasia lesions are located at the bottom of a deep sulcus. Brain 131, 3246–3255.

Bien, C.G., Szinay, M., Wagner, J., Clusmann, H., Becker, A.J., Urbach, H., 2009. Characteristics and surgical outcomes of patients with refractory magnetic resonance imaging-negative epilepsies. Arch. Neurol. 66, 1491–1499.

Blumcke, I., Spreafico, R., Haaker, G., Coras, R., Kobow, K., Bien, C.G., Pfäfflin, M., Elger, C., Widman, G., Schramm, J., Becker, A., Braun, K.P., Leijten, F., Baayen, J.C., Aronica, E., Chassoux, F., Hamer, H., Stefan, H., Rössler, K., Thom, M., Walker, M.C., Sisodiya, S.M., Duncan, J.S., McEvoy, A.W., Pieper, T., Holthausen, H., Kudernatsch, M., Meencke, H.J., Kahane, P., Schulze-Bonhage, A., Zentner, J., Heiland, D.H., Urbach, H., Steinhoff, B.J., Bast, T., Tassi, L., Lo, R.G., Özkara, C., Oz, B., Krsek, P., Vogelgesang, S., Runge, U., Lerche, H., Weber, Y., Honavar, M., Pimentel, J., Arzimanoglou, A., Ulate-Campos, A., Noachtar, S., Hartl, E., Schijns, O., Guerrini, R., Barba, C., Jacques, T.S., Cross, J.H., Feucht, M., Mühlebner, A., Grunwald, T., Trinka, E., Winkler, P.A., Gil-Nagel, A., Toledano, D.R., Mayer, T., Lutz, M., Zountsas, B., Garganis, K., Rosenow, F., Hermsen, A., von, O.T.J., Diepgen, T.L., Avanzini, G., 2017. Histopathological Findings in Brain Tissue Obtained during Epilepsy Surgery. N Engl J Med 377, 1648–1656.

Blümcke, I., Thom, M., Aronica, E., Armstrong, D.D., Vinters, H.V., Palmini, A., Jacques, T.S., Avanzini, G., Barkovich, A.J., Battaglia, G., Becker, A., Cepeda, C., Cendes, F., Colombo, N., Crino, P., Cross, J.H., Delalande, O., Dubeau, F., Duncan, J., Guerrini, R., Kahane, P., Mathern, G., Najm, I., Ozkara, C., Raybaud, C., Represa, A., Roper, S.N., Salamon, N., Schulze-Bonhage, A., Tassi, L., Vezzani, A., Spreafico, R., 2011. The clinicopathologic spectrum of focal cortical dysplasias: a consensus classification proposed by an ad hoc Task Force of the ILAE Diagnostic Methods Commission. Epilepsia 52, 158–174.

Carandini, M., Heeger, D.J., 2011. Normalization as a canonical neural computation. Nat. Rev. Neurosci. 13, 51–62.

Cohen, J., 1988. Statistical power analysis for the behavioral sciences. L. Erlbaum Associates, Hillsdale, N.J.

Cox, R.W., 1996. AFNI: software for analysis and visualization of functional magnetic resonance neuroimages. Comput Biomed Res 29, 162–173.

Dale, A.M., Fischl, B., Sereno, M.I., 1999. Cortical surface-based analysis. I. Segmentation and surface reconstruction. Neuroimage 9, 179–194.

Fischl, B., Sereno, M.I., Dale, A.M., 1999. Cortical surface-based analysis. II: Inflation, flattening, and a surface-based coordinate system. Neuroimage 9, 195–207.

Ganzetti, M., Wenderoth, N., Mantini, D., 2016. Intensity Inhomogeneity Correction of Structural MR Images: A Data-Driven Approach to Define Input Algorithm Parameters. Front. Neuroinform. 10, 10.

Glasser, M.F., Essen, D.C.V., 2011. Mapping Human Cortical Areas In Vivo Based on Myelin Content as Revealed by T1- and T2-Weighted MRI. J. Neurosci. 31, 11597–11616.

Glasser, M.F., Van, E.D.C., 2011. Mapping human cortical areas in vivo based on myelin content as revealed by T1- and T2-weighted MRI. J. Neurosci. 31, 11597–11616.

Hong, S.J., Bernhardt, B.C., Caldairou, B., Hall, J.A., Guiot, M.C., Schrader, D., Bernasconi, N., Bernasconi, A., 2017. Multimodal MRI profiling of focal cortical dysplasia type II. Neurology 88, 734–742.

Hong, S.J., Kim, H., Schrader, D., Bernasconi, N., Bernhardt, B.C., Bernasconi, A., 2014. Automated detection of cortical dysplasia type II in MRI-negative epilepsy. Neurology 83, 48–55.

Huppertz, H.J., Grimm, C., Fauser, S., Kassubek, J., Mader, I., Hochmuth, A., Spreer, J., Schulze-Bonhage, A., 2005. Enhanced visualization of blurred gray-white matter junctions in focal cortical dysplasia by voxel-based 3D MRI analysis. Epilepsy Res. 67, 35–50.

Jin, B., Krishnan, B., Adler, S., Wagstyl, K., Hu, W., Jones, S., Najm, I., Alexopoulos, A., Zhang, K., Zhang, J., Ding, M., Wang, S., Wang, Z.I., 2018. Automated detection of focal cortical dysplasia type II with surface-based magnetic resonance imaging postprocessing and machine learning. Epilepsia 59, 982–992.

Joyseeree, R., Müller, H., Depeursinge, A., 2018. Rotation-covariant tissue analysis for interstitial lung diseases using learned steerable filters: Performance evaluation and relevance for diagnostic aid. Comput. Med. Imaging Graph. 64, 1–11.

Kini, L.G., Gee, J.C., Litt, B., 2016. Computational analysis in epilepsy neuroimaging: A survey of features and methods. Neuroimage Clin. 11, 515–529.

Laparra, V., Camps-Valls, G., Malo, J., 2011. Iterative Gaussianization: from ICA to random rotations. IEEE Trans. Neural. Netw. 22, 537–549.

Lerner, J.T., Salamon, N., Hauptman, J.S., Velasco, T.R., Hemb, M., Wu, J.Y., Sankar, R., Donald, S.W., Engel, J.J., Fried, I., Cepeda, C., Andre, V.M., Levine, M.S., Miyata, H., Yong, W.H., Vinters, H.V., Mathern, G.W., 2009. Assessment and surgical outcomes for mild type I and severe type II cortical dysplasia: a critical review and the UCLA experience. Epilepsia 50, 1310–1335.

Martin, P., Winston, G.P., Bartlett, P., de, T.J., Duncan, J.S., Focke, N.K., 2017. Voxel-based magnetic resonance image postprocessing in epilepsy. Epilepsia 58, 1653–1664.

Nieuwenhuys, R., Broere, C.A., 2017. A map of the human neocortex showing the estimated overall myelin content of the individual architectonic areas based on the studies of Adolf Hopf. Brain Struct. Funct. 222, 465–480.

Paquola, C., Vos, D.W.R., Wagstyl, K., Bethlehem, R.A.I., Hong, S.J., Seidlitz, J., Bullmore, E.T., Evans, A.C., Misic, B., Margulies, D.S., Smallwood, J., Bernhardt, B. C., 2019. Microstructural and functional gradients are increasingly dissociated in transmodal cortices. PLoS Biol. 17, e3000284.

Pedregosa, F., Varoquaux, G., Gramfort, A., Michel, V., Thirion, B., Grisel, O., Blondel, M., Prettenhofer, P., Weiss, R., Dubourg, V., Vanderplas, J., Passos, A., Cournapeau, D., Brucher, M., Perrot, M., Duchesnay, E., 2011. Scikit-learn: Machine Learning in Python. J. Mach. Learn. Res. 12, 2825–2830.

Portilla, J., Strela, V., Wainwright, M.J., Simoncelli, E.P., 2003. Image denoising using scale mixtures of Gaussians in the wavelet domain. IEEE Trans. Image Process 12, 1338–1351.

Selvaganesan, K., Whitehead, E., DeAlwis, P.M., Schindler, M.K., Inati, S., Saad, Z.S., Ohayon, J.E., Cortese, I.C.M., Smith, B., Steven, J., Nath, A., Reich, D.S., Inati, S., Nair, G., 2019. Robust, atlas-free, automatic segmentation of brain MRI in health and disease. Heliyon 5, e01226.

Simoncelli, E.P., Olshausen, B.A., 2001. Natural image statistics and neural representation. Annu. Rev. Neurosci. 24, 1193–1216.

Triarhou, L.C., 2007. The Economo-Koskinas atlas revisited: cytoarchitectonics and functional context. Stereotact. Funct. Neurosurg. 85, 195–203.

Téllez-Zenteno, J.F., Hernández, R.L., Moien-Afshari, F., Wiebe, S., 2010. Surgical outcomes in lesional and non-lesional epilepsy: a systematic review and meta-analysis. Epilepsy Res. 89, 310–318.

Thesen, T., Quinn, B.T., Carlson, C., Devinsky, O., DuBois, J., McDonald, C.R., French, J., Leventer, R., Felsovalyi, O., Wang, X., Halgren, E., Kuzniecky, R., 2011. Detection of epileptogenic cortical malformations with surface-based MRI morphometry. PLoS One. 6 (2), e16430.

Wagner, J., Weber, B., Urbach, H., Elger, C.E., Huppertz, H.J., 2011. Morphometric MRI analysis improves detection of focal cortical dysplasia type I. Brain 134, 2844–2854.

Wang, Q., Zheng, Y., Yang, G., Jin, W., Chen, X., Yin, Y., 2018. Multiscale Rotation-Invariant Convolutional Neural Networks for Lung Texture Classification. IEEE J. Biomed. Health Inform. 22, 184–195.

Wang, Z.I., Jones, S.E., Jaisani, Z., Najm, I.M., Prayson, R.A., Burgess, R.C., Krishnan, B., Ristic, A., Wong, C.H., Bingaman, W., Gonzalez-Martinez, J.A., Alexopoulos, A.V., 2015. Voxel-based morphometric magnetic resonance imaging (MRI) postprocessing in MRI-negative epilepsies. Ann. Neurol. 77, 1060–1075.

Zacharaki, E.I., Wang, S., Chawla, S., Soo, Y.D., Wolf, R., Melhem, E.R., Davatzikos, C., 2009. Classification of brain tumor type and grade using MRI texture and shape in a machine learning scheme. Magn. Reson. Med. 62, 1609–1618.

Zilles, K., Amunts, K., 2010. Centenary of Brodmann's map–conception and fate. Nat. Rev. Neurosci. 11, 139–145.